Unsupervised restoration of brain SPECT volumes

Max Mignotte • ‡ Jean Meunier •

• DIRO, Département d'Informatique et de Recherche Opérationnelle,
P.O. 6128, succ. Centre-ville, Montréal, Canada (Québec), H3C3J7.

‡ INRIA, Institut National de Recherche en Informatique et Automatique, France.

Abstract

Thanks to its ability to yield functionally-based information, the three-dimensional (3D) SPECT imagery technique has become a great help in the diagnostic of cerebrovascular diseases. Nevertheless, due to the imaging process, the 3D SPECT images are blurred and consequently their interpretation by the clinician is often difficult. In order to improve the resolution of these images and then to facilitate their interpretation, we propose herein, to extend a recent image blind deconvolution technique (called the NAS-RIF technique) in order to improve both the spatial and the inter-slice resolution of SPECT volumes. This scheme requires a preliminary step in order to find the support of the object to be restored. In this paper, we propose to solve this problem thanks to an unsupervised 3D Markovian segmentation technique. This method has been successfully tested on numerous real and simulated brain SPECT volumes, yielding very promising restoration results[1].

1 Introduction

3D SPECT (Single Photon Emission Computed Tomography) images are obtained by the detection of radiations (gamma rays) coming from radioactive isotopes injected in the human body. Contrary to other medical imaging techniques, such as X-ray, CT (Computer Tomography), MRI (Magnetic Resonance Imaging), etc., this imagery process is able to give functionally rather than anatomically-based information, such as the 3D metabolic behavior of human brain, by visualizing the level of blood flow of a set of cross-sectional images. This study of regional Cerebral Blood Flow (rCBF) can aid in the diagnostic of cerebrovascular diseases (e.g., Alzheimer's disease, Parkinson's disease, etc.) by indicating lower, or abnormal higher, 3D metabolic activity in some brain regions.

[1]**Acknowledgements :** The authors thank INRIA (Institut National de la Recherche en Informatique et Automatique, France) for financial support of this work (postdoctoral grant). The authors are also grateful to Jean-Paul Soucy and Christian Janicki (CHUM, University of Montreal) for having provided the SPECT images.

Due to the imaging process, SPECT suffers from poor spatial resolution mainly owing to the 3D scattering of the emitted photons. Consequently, resulting 3D SPECT images are very blurred and their interpretation by the nuclear physician is often difficult and subjective. If the object to be visualized is small compared to the source-to-collimator distance, this degradation phenomenon may be considered to be shift-invariant [1] and, neglecting noise, this one can be modeled by a 3D convolution process between the true undistorted 3D image and the transfer function of the imaging system (also called the Point Spread Function or PSF).

In order to improve the spatial resolution of SPECT volumes, some authors have thus investigated the SPECT image deblurring problem by neglecting the inter-slice blur and by approximating this transfer function with a 2D symmetric Gaussian function [2, 3] or by considering an a priori known PSF [4]. In this context, classical Wiener filter techniques [1, 2] or maximum entropy filter-based deconvolution technique [4] have then been proposed to achieve this deconvolution procedure and significant resolution improvements have been noticed [1, 2, 4]. Nevertheless, let us note that these methods don't take into account the inter-slice blur inherent to this 3D SPECT imagery process and are sensitive to the assumption made on the nature of the blurring function. In our applications where little is known about the PSF, it can turn out to be more relevant to estimate directly the PSF from the observed input image. This problem of simultaneously estimating the PSF and restoring an unknown image is called a "blind deconvolution" problem. Recent 2D deconvolution techniques exist, such as the NAS-RIF algorithm, and can also be efficiently extended in the 3D SPECT imagery context. These techniques require to find, in a preliminary step, the support of the object to be restored. In this paper, we propose to solve this problem thanks to an unsupervised 3D Markovian segmentation technique.

This paper is organized as follows. Section 2 describes the proposed 3D extension of the NAS-RIF deconvolution technique. In Section 3, we detail the 3D unsupervised Markovian segmentation algorithm allowing to find the support of the object to be restored. Deconvolution results on phantoms and real SPECT volumes are given in Section 4.

2 3D Deconvolution Method

In our application, the degradation of a SPECT volume can be represented as the result of a convolution of the true volume with a 3D blurring function (the PSF), plus an additive term to model the noise from the physical system. If the imaging system is assumed to be linear and shift invariant, this degradation process can then be expressed by the following linear model,

$$g(x,y,z) = f(x,y,z) * h(x,y,z) + n(x,y,z),$$

where $g(x,y,z)$ is the degraded or blurred 3D image, $f(x,y,z)$ is the undistorted true 3D image, $h(x,y,z)$ is the PSF of the imaging system and $n(x,y,z)$ is the corrupting noise (assumed additive in our model). In this notation, the coordinates (x,y) represent the discrete pixel spatial locations, z the slice location and $*$ designates the 3D discrete linear convolution operator. The 3D blind deconvolution problem consists then in determining $f(x,y,z)$ and $h(x,y,z)$ given the blurred observation $g(x,y,z)$.

When the object to be recovered is imaged against a uniform or a noisy background, a commonly used method for solving a 2D blind deconvolution problem consists in minimizing an error metric that optimizes the form of the restored image and the PSF (or its inverse) to fit the various constraints, *a priori* known, on the form of the solution; typically positivity and known support of the object. The steepest descent or conjugate gradient method are then generally used to achieve optimization [5, 6]. In our application, the true undistorted rCBF map of a human brain consists of a finite support imaged against a noisy background due to the Poisson noise phenomenon. Assuming that this support is *a priori* known or previously estimated, we can use a 3D extension of such deconvolution technique for improving both spatial and inter-slice resolution of SPECT volumes.

In this context, the recent Non-negativity and Support constraints Recursive Inverse Filtering (NAS-RIF) algorithm [5] can efficiently be extended. We can derive a 3D extension of this technique by simply considering a 3D variable FIR filter $u(x,y,z)$ of dimension $N_x \times N_y \times N_z$ with the blurred SPECT volume pixels $g(x,y,z)$ as input (cf. Fig. 1). The output of this filter gives an estimate of each cross-sectional 2D true image $\hat{f}(x,y,z=k)$ (with $k \in [1,K]$ and K is the number of transversal slices in the volume). Each resulting estimation is passed through a nonlinear filter which uses a non-expansive mapping to project the estimated 2D image into the space representing the known characteristics of the true image. The difference between this projected image $\hat{f}_{\text{NL}}(x,y,z=k)$ and $\hat{f}(x,y,z=k)$ is used as the error signal to update the variable filter $u(x,y,z)$. Fig. 1 gives an overview of the proposed 3D-extended NAS-RIF deconvolution algorithm. Each cross-sectional 2D image is assumed to be non-negative with known support. The cost function used in the deconvolution procedure of the k^{th} transversal 2D image is defined as,

$$J_k = \sum_{(x,y)\in\mathcal{D}_{[k]}} \hat{f}^2(x,y,z=k)\left(\frac{1-\text{sgn}(\hat{f}(x,y,z=k))}{2}\right) + \sum_{(x,y)\in\overline{\mathcal{D}}_{[k]}} \left(\hat{f}(x,y)-L_{\text{B}}\right)^2 + \gamma\left(\sum_{\forall(x,y,z)} u(x,y,z)-1\right)^2,$$

where $\hat{f}(x,y,z) = g(x,y,z) * u(x,y,z)$, and $\text{sgn}(f) = -1$ if $f < 0$ and $\text{sgn}(f) = 1$ if $f \geq 0$. $\mathcal{D}_{[k]}$ and $\overline{\mathcal{D}}_{[k]}$ is the set of all pixels of $g(x,y,z=k)$ inside and outside the region of support respectively. The variable γ in the third term is nonzero only when L_{B} is zero, i.e., the background color is black. The third term is used to constrain the parameter away from the trivial all-zero global minimum for this situation. The authors have shown in [5] that the above equation is convex in the 2D case with respect to u. This property remains true in the 3D case so that convergence of the algorithm to the global minimum is ensured using the conjugate gradient minimization routine [5]. Let us note that a fully 3D deconvolution scheme would consist in minimizing directly the cost function $J = \sum_{k=1}^{K} J_k$. Nevertheless, J_k and J being convex and the global minimum being ensured in both cases by the conjugate gradient optimization routine, the estimated solutions are thus identical.

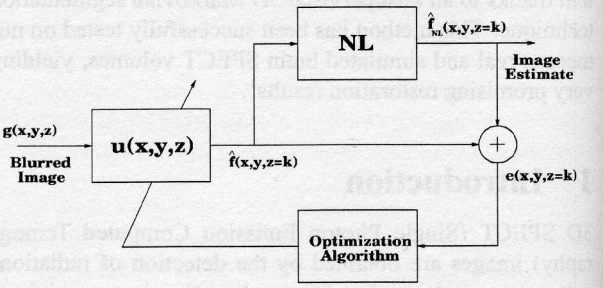

Figure 1: 3D extension of the NAS-RIF algorithm.

3 Support determination method

In the 2D case, the support can be roughly approximated by the smallest rectangle containing the entire object [5]. In order to automatically determine this rectangular frame, some of the proposed methods are based on hold-out methods [5], or inspired by the constraint assessment algorithm proposed in [7]. These methods are reliable for assessing the optimal 2D rectangular support but cannot be easily extended in order to define a more accurate segmentation. An alternative approach consists in exploiting the result of a 3D unsupervised Markovian segmentation using a two step process: first, a parameter estimation step in which we have to

estimate the MRF model parameter. Then, a second step devoted to the segmentation itself based on the values of the estimated parameters.

To this end, we consider a couple of random fields $Z = (X, G)$, where $G = \{G_s, s \in S\}$ represents the field of observations located on the 3D lattice S consisting of K lattices S_k of N sites s (associated to the N pixels of each transversal slice of the volume), and $X = \{X_s, s \in S\}$ the label field (related to the $K \times N$ class labels X_s of a segmented volume). Each aforementioned label is associated to a specific brain anatomical tissue or region of the SPECT volume; the "CSF" area designates the region that is normally due to the lack of radiations. In this MRF model parameter estimation and segmentation problems, this region designates the brain region filled with Cerebrospinal Fluid (without blood flow and thus without radiation) and also the area outside the brain region. The "white matter" and "grey matter" (brightest region) are associated to a low and a higher level of blood flow respectively [8]. Each G_s takes its value in $\{0, \ldots, 255\}$ (256 grey levels), and each X_s in $\{e_1 = \text{"CSF"}, e_2 = \text{"white matter"}, e_3 = \text{"grey matter"}\}$.

The distribution of (X, G) is defined, firstly, by prior distribution $P_X(x)$, supposed to be Markovian and secondly, by the conditional likelihoods $P_{G_s/X_s}(g_s/x_s)$ whose shape and parameter vector $\Phi_{(x_s)}$ depends on the concerned class label x_s. In order to take into account the Poisson noise phenomenon inherent to the SPECT imaging process in the "CSF" area, we model $P_{G_s/X_s}(g_s/e_1)$, by a exponential law [3] with parameter α, namely; $(1/\alpha)\exp[-(g_s/\alpha)]$. To describe the brightness within the "white matter" and the "grey matter" regions, we model the conditional density function for these two regions by two different Gaussian laws [3]. The observable G is called the "incomplete data" whereas Z constitutes the "complete data".

Estimation Step

In order to determine $\Phi = (\Phi_{(e_1)}, \Phi_{(e_2)}, \Phi_{(e_3)})$, we use the Iterative Conditional Estimation (ICE) algorithm. This estimation procedure [9] relies on an estimator $\hat{\Phi}(X, G)$ of the "complete data". This iterative method starts from an initial parameter vector $\Phi^{[0]}$ and generates a sequence of parameter vectors leading to the optimal parameters, in the least squares sense, with the following iterative scheme,

$$\Phi^{[p+1]} = \frac{1}{n}\left[\hat{\Phi}(x_{(1)}, g) + \cdots + \hat{\Phi}(x_{(n)}, g)\right],$$

where $x_{(i)}, i = 1, \ldots, n$ are realizations of X drawn according to the posterior distribution $P_{X/G}(x/g, \Phi^{[p]})$. In order to decrease the computational load, we can take $n = 1$ without altering the quality of the estimation [9]. Finally, we can use the Gibbs sampler algorithm [10] to simulate realizations of X according to the posterior distribution. For the local *a priori* model of the Gibbs sampler, we adopt a 3D isotropic Potts model with a first order neighborhood [11]. In this model, there are three parameters denoted $\beta_1, \beta_2, \beta_3$, called "the clique parameters" [11], and associated to the horizontal, vertical, and transverse binary cliques respectively [3]. Given this *a priori* model, the prior distribution $P_X(x)$ can be written as,

$$P_X(x) = \exp\Big(-\sum_{<s,t>} \beta_{st}(1 - \delta(x_s, x_t))\Big),$$

where summation is taken over all pairs of spatial and inter-level neighboring sites and δ is the Kronecker delta function. In order to favor homogeneous regions with no privileged orientation in the Gibbs sampler simulation process, we choose $\beta_{st} = \beta_1 = \beta_2 = \beta_3 = 1$. Finally, $\Phi^{[p+1]}$ is computed from $\Phi^{[p]}$ in the following way,

- **Stochastic Step**: using the Gibbs sampler, one realization x is simulated according to the posterior distribution $P_{X/G}(x/g)$, with parameter vector $\Phi^{[p]}$.
- **Estimation Step**: the parameter vector $\Phi^{[p+1]}$ is estimated with the Maximum Likelihood (ML) estimator of the "complete data" corresponding to each class:
  - If $N_1 = \#\{s \in S : x_s = e_1\}$ is the number of pixels of the "CSF" area, the ML estimator $\hat{\Phi}_{(e_1)}$ of α is given by [12]: $\hat{\alpha}(x, g) = (1/N_1)\sum_{s \in S: x_s = e_1} g_s$.
  - If $N_2 = \#\{s \in S : x_s = e_2\}$ and $N_3 = \#\{s \in S : x_s = e_3\}$ pixels are located in the "white matter" and "grey matter" regions respectively, the corresponding ML estimator of each class is given by the empirical mean and the empirical variance. For instance, for the "white matter" class, we have for $\hat{\Phi}_{(e_2)}$,

$$\hat{\mu}(x, g) = \frac{1}{N_2}\sum_{s \in S: x_s = e_2} g_s,$$

$$\hat{\sigma}^2(x, g) = \frac{1}{(N_2 - 1)}\sum_{s \in S: x_s = e_2} (g_s - \hat{\mu})^2.$$

- Repeat until convergence is achieved; i.e., if $\hat{\Phi}^{[p+1]} \not\approx \hat{\Phi}^{[p]}$, we return to Stochastic Step.

Fig. 2 and Table 1 represent the estimated distribution mixture and corresponding estimates of the SPECT volume shown in Fig. 3.

Segmentation Step

Based on these estimates, we can compute a 3D Markovian segmentation of SPECT volumes. In this framework, the Markovian segmentation can be viewed as a statistical labeling problem according to a global Bayesian formulation in which the posterior distribution $P_{X/G}(x/g) \propto$

[3] Cliques are subsets of site(s) which are mutual neighbors [11].

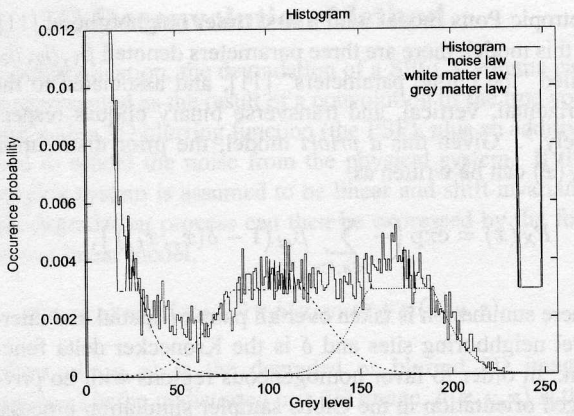

Figure 2: Image histogram of the picture reported in Fig. 3 (solid curve) and estimated probability density mixture obtained with the ICE procedure (dotted and dashed curves).

	ICE Procedure		
$\Phi^{\text{final}}_{(e_1)}$	$0.52_{(\pi)}$	$11_{(\alpha)}$	
$\Phi^{\text{final}}_{(e_2)}$	$0.26_{(\pi)}$	$100_{(\mu)}$	$648_{(\sigma^2)}$
$\Phi^{\text{final}}_{(e_3)}$	$0.22_{(\pi)}$	$172_{(\mu)}$	$383_{(\sigma^2)}$

Table 1: Estimated parameters for the SPECT volume reported in Fig. 3. π stands for the proportion of the three classes within the volume. α are the exponential law parameter. μ and σ^2 are the Gaussian law parameters.

$\exp -U(x,g)$ has to be maximized [11]. The corresponding posterior energy is,

$$U(x,g) = \underbrace{\sum_{s\in S} -\ln P_{G_s/X_s}(g_s/x_s)}_{U_1(x,g)} + \underbrace{\sum_{<s,t>} \beta_{st}\left(1-\delta(x_s,x_t)\right)}_{U_2(x)},$$

where U_1 expresses the adequacy between observations and labels, and U_2 represents the energy of the *a priori* model. We use the deterministic Iterated Conditional Modes (ICM) algorithm [11] to minimize this energy function. Fig. 3 displays examples of unsupervised three-class segmentation. In this segmentation, the "CSF", the "white matter" and the "grey matter" are represented by a dark, a grey, and a white region respectively. The support $\mathcal{D}$ is then determined simply by the set of pixels belonging to the white and grey matter classes.

4 Experimental results

The effectiveness of this 3D blind deconvolution method was tested on several SPECT volumes composed of 64 transversal slices of 64×64 pixels with 256 grey levels. Those presented herein are only a few examples. The initial inverse FIR filter required by the NAS-RIF algorithm is the Kronecker delta function [5] and the size of this inverse filter is $3\times3\times3$ pixels. Besides, we have used $\gamma = 0$ because the background of SPECT images is not completely black. The computational cost on a standard SunSparc 2 is about 20 seconds for the support determination of the whole volume and 30 seconds for the blind deconvolution of each cross-sectional image.

Fig. 4 presents an example of SPECT volume blind deconvolution. The algorithm converges to a very good estimate of the solution without *a priori* information on the PSF and allows to noticeably improve the resolution of the original SPECT volume. Fig. 5 shows the resolution improvement obtained by the 3D-extended version of the NAS-RIF algorithm over its 2D version for a given cross-sectional image. Fig. 6 shows an example of sagittal and coronal sections of the original and deconvolved brain SPECT volume whose cross-sectional slices have been presented in Fig. 4. The improvement of the inter-slice resolution is also clearly visible.

The effectiveness of this deconvolution technique is also tested on a real SPECT phantom (i.e., a physical plexiglas head phantom filled with radioactive material and measured by a SPECT system) for which the ground truth of this segmented phantom is exactly known and thus for which the performance of our proposed method can then be objectively judged. Fig. 7 presents examples of blind deconvolutions on this SPECT phantom. We can notice that this SPECT volume is less noisy and less blurred than the real SPECT volume previously processed (due to several factors such as a different dose of radioactive isotopes contained in each uniform region of this SPECT phantom, a longer acquisition time, the stillness of this simulated brain during the SPECT process, etc.). In order to fully assess the success of this restoration procedure, we use the specific evaluation criteria proposed in [4], based on the estimation of the two following measures:

(i) Firstly, the average contrast of the image, defined by $C = (1 - m_2/m_3)$, where m_2 and m_3 are the mean of the pixel value in the "white matter" and "grey matter" area respectively.

(ii) Secondly, the image mottle $M = \rho_2 M_2 + \rho_3 M_3$. M_2 and M_3 designate the ratio of the standard deviation of pixel values to the mean in the "white matter" and "grey matter" area respectively. ρ_2 and ρ_3 designate the proportion of pixel belonging to each class.

This last parameter allows to measure the amplification

of the noise and/or measure the presence of undesirable artifacts that can be created by the deconvolution procedure in a uniform region of the real SPECT phantom. A reliable SPECT image restoration technique will then allow to enhance the contrast of the image with little increase in mottle, i.e., without amplifying too much the noise and/or without creating false artificial features (technically, an increase by a factor of $1.1-1.2$ of the original mottle of the image remains acceptable if the contrast enhancement is significantly increased [4]). Due to the difference of thickness between the cross-sectional slices of the real and segmented phantom, these abovementioned measures are estimated on the whole 3D phantom after this one has been registered [13] on the ground truth of the segmented phantom volume. Our proposed restoration technique allows a contrast enhancement from 9% to 21% between the original and deconvolved SPECT phantom along with an acceptable amplification of the mottle by a factor of 1.18 (from 17% to 20%). This represents a significant improvement in image quality with a very small penalty and attest the validity of this restoration method.

Finally, we have also tested our 3D deconvolution technique on a cross-sectional slice of a synthetic SPECT volume. In order to simulate at best the typical characteristics of real brain SPECT images, we have re-created three homogeneous regions and added the corresponding noise for each ones, according to the grey level distribution already estimated on a real brain SPECT volume (cf. Fig. 2 and Table 1). We have also added a 3D Gaussian blur in order to simulate the 3D scattering of the emitted photons. Fig. 8 shows the obtained deconvolution result. The resolution improvement is visible and the proposed procedure allow efficiently to recover high frequencies of the undistorted (non-convolved) image.

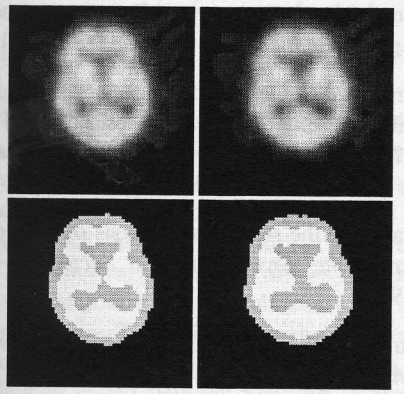

Figure 3: Example of an unsupervised 3D Markovian segmentation of a brain SPECT volume using the ICM algorithm and based on the parameters estimated by the ICE procedure. Top: real brain SPECT volume (two central transversal slices). Bottom: three-class Markovian segmentations.

5 Conclusion

In this paper we have shown that a 3D extension of the NAS-RIF deconvolution procedure noticeably improves the resolution of 3D SPECT images and can be a great help to facilitate their interpretation by the nuclear physician. We have also shown that this 3D blind deconvolution technique gives superior performance than its 2D version and can efficiently exploit the result of a 3D unsupervised Markovian segmentation in order to find the exact support of the object to be restored. Finally, this 3D blind deconvolution technique combined with this unsupervised segmentation leads to a restoration procedure that is completely data driven and really compatible with an automatic processing of massive amounts of 3D SPECT data.

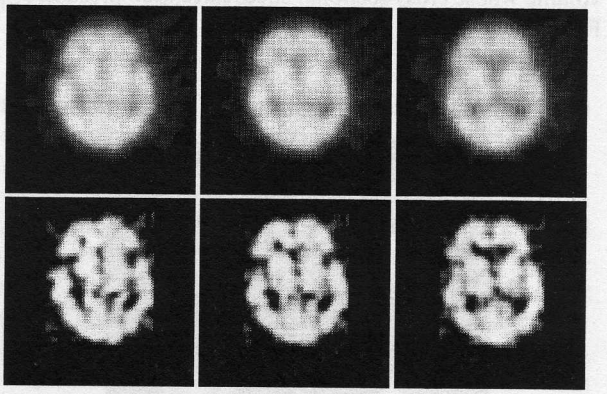

Figure 4: Examples of human brain SPECT volume deconvolution given by the 3D-extended version of the NAS-RIF algorithm combined with the Markovian segmentation-based support finding algorithm. Top: three consecutive real cross-sectional SPECT slices. Bottom: deconvolution results.

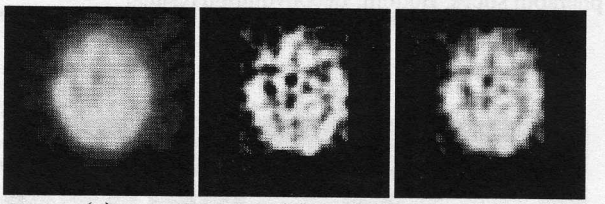

(a) (b) (c)

Figure 5: Examples of human brain SPECT cross-sectional image deconvolutions. (**a**) Original SPECT cross-sectional human brain image. (**b**) Deconvolution result given by the 3D-extended version of the NAS-RIF algorithm (inverse filter size is $3\times3\times3$). (**c**) Deconvolution result given by its 2D version (inverse filter size is 5×5). Both deconvolution methods require the same computational load and are combined with the proposed Markovian segmentation-based support-finding algorithm.

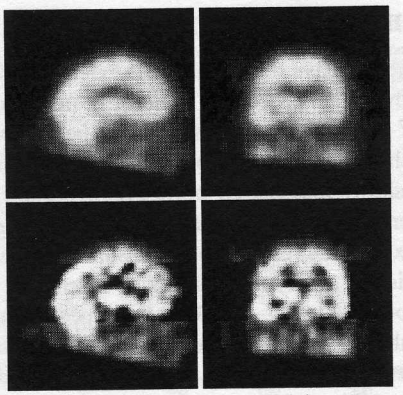

(a) (b)

Figure 6: Example of sagittal (**a**) and coronal (**b**) sections of the original (top) and deconvolved (bottom) brain SPECT volume whose cross-sectional slices have been presented in Fig. 4.

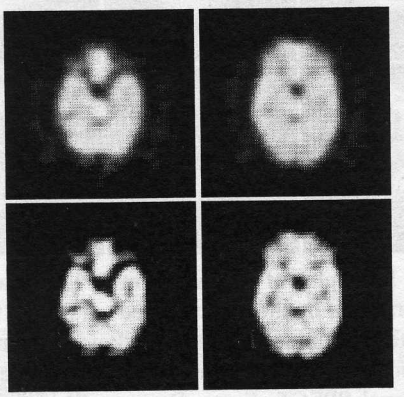

Figure 7: Examples of deconvolution obtained by our 3D blind deconvolution technique on two cross-sectional slices of a SPECT phantom. Top: real cross-sectional SPECT phantom slices. Bottom: deconvolution results.

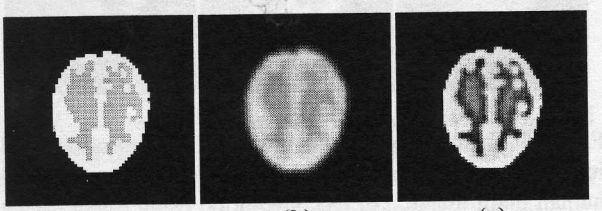

(a) (b) (c)

Figure 8: Example of deconvolution result on a cross-sectional slice of a synthetic SPECT volume. (**a**) Ground truth of the segmented synthetic slice. (**b**) Synthetic SPECT slice. (**c**) Deconvolution result.

References

[1] D. Boulfelfel, R.M. Rangayyan, L.J. Han, and R. Kloiber. Prereconstruction restoration of myocardial single photon emission computed tomography images. *IEEE Trans. on Medical Imaging*, 11(3):336–341, 1992.

[2] M.T. Madsen and C.H. Park. Enhancement of SPECT images by Fourier filtering the projection set. *Journal of Nuclear Science*, 26:2687–2690, 1979.

[3] T.S. Curry, J.E. Dowdey, and R.C. Murry. *Christensen's Physics of Diagnostic Radiology*. Lea and Febiger, 1990.

[4] S. Webb, A.P. Long, R.J. Ott, M.O. Leach, and M.A. Flower. Constrained deconvolution of SPECT liver tomograms by direct digital image restoration. *Medical Physic*, 12(1):53–58, 1985.

[5] D. Kundur and D. Hatzinakos. Blind image restoration via recursive filtering using deterministic constraints. In *Proc. International Conference on Acoustics, Speech, and Signal Processing*, volume 4, pages 547–549, 1996.

[6] Y.L. You and M. Kaveh. A regularization approach to joint blur identification and image restoration. *IEEE trans. on Image Processing*, 5(3):416–428, 1996.

[7] S. J. Reeves and M. Mersereau. Automatic assessment of constraint sets in image restoration. *IEEE Trans. on Image Processing*, 1(1):119–123, 1992.

[8] D.C. Costa and P.J. Ell. *Brain Blood Flow in Neurology and Psychiatry*. Series Editor: P.J. Ell, 1991.

[9] B. Braathen, P. Masson, and W. Pieczynski. Global and local methods of unsupervised Bayesian segmentation of images. *Graphics and Vision*, 2(1):39–52, 1993.

[10] S. Geman and D. Geman. Stochastic relaxation, Gibbs distributions and the Bayesian restoration of images. *IEEE Trans. on Pattern Analysis and Machine Intelligence*, 6(6):721–741, 1984.

[11] J. Besag. On the statistical analysis of dirty pictures. *Journal of the Royal Statistical Society*, B-48:259–302, 1986.

[12] S. Banks. *Signal processing, image processing and pattern recognition*. Prentice Hall, 1990.

[13] K.J. Friston, J. Ashburner, C.D. Frith, J.B. Poline, J.D. Heather, and R.S.J. Frackowiak. Spatial registration and normalization of images. *Human Brain Mapping*, 3(3):165–189, 1995.